POLITECNICO DI TORINO
Repository ISTITUZIONALE

Analysis of H-mode and L-mode plasmas with a liquid Sn CPS divertor test unit in the ASDEX Upgrade tungsten divertor

Original
Analysis of H-mode and L-mode plasmas with a liquid Sn CPS divertor test unit in the ASDEX Upgrade tungsten divertor / Bray, E., Fajardo, D., Angioni, C., Samoylov, O., Dux, R., Nallo, G.F., Marchetto, C., Subba, F.. - In: NUCLEAR MATERIALS AND ENERGY. - ISSN 2352-1791. - 47:(2026). [10.1016/j.nme.2026.102121]

Availability:
This version is available at: 11583/3010688 since: 2026-05-08T15:00:06Z

Publisher:
Elsevier Ltd

Published
DOI:10.1016/j.nme.2026.102121

Terms of use:

This article is made available under terms and conditions as specified in the corresponding bibliographic description in the repository

Publisher copyright

(Article begins on next page)

15 October 2026

Nuclear Materials and Energy 47 (2026) 102121

Contents lists available at ScienceDirect

Nuclear Materials and Energy

journal homepage: www.elsevier.com/locate/nme

Analysis of H-mode and L-mode plasmas with a liquid Sn CPS divertor test unit in the ASDEX Upgrade tungsten divertor☆

Elisabetta Bray [a,*], Daniel Fajardo [b], Clemente Angioni [b], Oleg Samoylov [b], Ralph Dux [b], Giuseppe F. Nallo [a], Chiara Marchetto [a], Fabio Subba [a], the ASDEX Upgrade team [b]

[a] NEMO Group - Energy Department, Politecnico di Torino, Corso Duca Degli Abruzzi 24, 10129 Turin, Italy
[b] Max–Planck-Institut für Plasmaphysik, 85748 Garching, Germany

ARTICLE INFO

Keywords:
Liquid metal divertor
Heavy impurities
Integrated modeling
ASTRA
Aurora

ABSTRACT

This study analyzes impurity transport during ASDEX Upgrade experiments in which a Liquid Tin Module (LTM) was exposed to diverted plasmas. Using ASTRA and Aurora, we interpret H-mode and L-mode discharges to assess tin penetration into the core and its impact on radiated power. In H-mode, the simulations reproduce the observed tin radiation and droplet ejection, resulting in core concentrations of $\sim 10^{-4}$ and significant radiated power fractions, incompatible with sustained performance. In contrast, L-mode conditions mitigate impurity accumulation even under comparable source strengths, highlighting the sensitivity of tin transport to background confinement and density. Nonetheless, droplet-induced bursts remain the dominant risk in both regimes.

Extrapolation to CPS-like (Capillary Porous Structure) divertor configurations suggests that uncontrolled droplet ejection could drive excessive radiation – especially in H-mode – whereas L-mode scenarios remain more tolerant. Overall, the results indicate that liquid tin divertors can be compatible with acceptable core performance, provided that effective strategies to suppress droplet ejection are implemented.

1. Introduction

Liquid Metal Divertors (LMD) are currently one of the possible solutions that can be adopted to address the issue of the power exhaust in tokamaks. Their positive outcomes include reducing the heat load at the target exploiting the so-called "self-healing" capability. The liquid metal flowing inside the Capillary Porous Structure (CPS) facing the plasma can evaporate producing a protective particle cloud above the surface. This vapor then condenses back into the porous structure, allowing the liquid to be replenished. In this way also mechanical stresses are reduced whilst the integrity and duration of the target are increased in time ([1,2]).

Tin (Sn) has been selected over lithium as liquid metal for the EU-DEMO conceptual design ([3,4]), primarily due to its ability to mitigate the accumulation of tritium inventory in the walls and reduce plasma dilution. Tin has previously been tested in linear plasma devices such as Magnum-PSI [2], and used as main limiter in tokamaks, including FTU [5] and NSTX [6]. While the above-mentioned experiments yielded promising results, a test in a tokamak with divertor configuration had never been performed before. This motivated the design of an experiment that exposed a single Liquid Tin Module (LTM) to a diverted plasma, to study its performance in terms of material redeposition and transport of particles through the plasma. The ASDEX Upgrade (AUG) tokamak has been selected for the purpose. This study focuses on the interpretation of this experimental campaign, and, specifically on the transport of impurities from the edge plasma to the core, estimating the resulting contamination.

The work is structured as follows: Section 2 provides a brief overview of the experimental setup, outlining the study's rationale and objectives. Section 3 then details the approach used to interpret the experimental results, leveraging the modeling capabilities of two different codes: ASTRA [7,8] and *Aurora* [9]. These codes are employed to interpret and model impurity transport and plasma behavior in the core region, with a more detailed discussion of the setup provided. The main results are presented in Section 4, followed by a discussion of the key conclusions in Section 5.

☆ This article is part of a Special issue entitled: 'PRD activities' published in Nuclear Materials and Energy.

* Corresponding author.
E-mail address: elisabetta.bray@polito.it (E. Bray).

https://doi.org/10.1016/j.nme.2026.102121
Received 7 January 2026; Received in revised form 10 March 2026; Accepted 7 April 2026
Available online 8 April 2026
2352-1791/© 2026 The Authors. Published by Elsevier Ltd. This is an open access article under the CC BY license (http://creativecommons.org/licenses/by/4.0/).

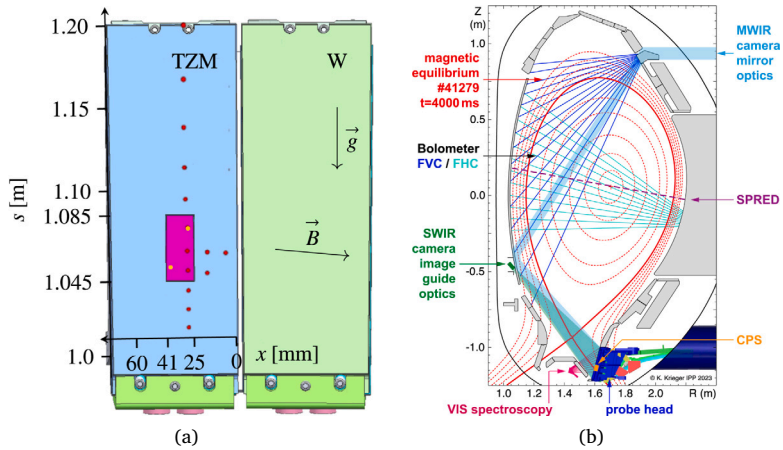

(a) (b)

Fig. 1. Frontal view of the LTM on the divertor tiles (left) and schematic representation of the diagnostics system (right), as from the work of J. Scholte [10]. Red and yellow dots represent the viewing points of diagnostics: the former indicating the location of the thermocouples, and the latter the Line of Sight (LoS) points of the FVS (divertor visible spectroscopy).

2. Experimental setup

A detailed description of the experimental setup is available in [10], hence only a brief summary shall be provided here. Fig. 1 (left) represents a front view of two divertor tiles where the LTM (in magenta) is located. It has dimensions of 40 mm × 16 mm × 25 mm and it is composed of a solid bulk made of tungsten, directly attached to a sintered porous layer, 1.5 mm thick, acting as the plasma-facing Capillary Porous Structure (CPS). The module is spring-loaded to ensure it remains aligned with a TZM (titanium-zirconium-molybdenum) divertor tile, while the surrounding tiles are made of tungsten. The porosity of the CPS is approximately 23 μm, which should effectively prevent the 1.5 g of liquid tin contained within the module from being ejected during operation, as indicated from previous studies [11].

During all the discharges of the campaign, the Outer Strike Point (OSP) was initially located above the CPS (top of Fig. 1, left). After approximately 2 s, it moved to a position directly over the LTM, where it remained for about 4 s before shifting away. When the OSP was not positioned over the LTM, only background radiation was observed. In contrast, when it was aligned with the LTM, impurity radiation became clearly pronounced.

Several diagnostics were employed to interpret the experimental results. Langmuir probes measured the temperature at the target, foil bolometers [12], specifically a horizontal (FHC) and a vertical (FVC) camera, were used to measure radiated power within the core plasma. Additionally, two spectrometers were used to obtain information on tin transitions: the SPRED (Survey, Poor Resolution, Extended Domain) [13] spectrometer for the vacuum ultraviolet (VUV) range, and the FVS (Divertor Visible Spectroscopy) spectrometer for the visible range.

3. Modeling strategy and simulation setup

The modeling activity was designed in order to reconstruct the plasma and impurity transport during the LTM discharges. Two shots were selected as reference cases: an H-mode pulse (#41279), where higher power and transient ELM activity enhance sputtering and impurity release, and an L-mode pulse (#41271), characterized by low auxiliary heating. In particular, the H-mode case offers insight into impurity behavior under strong plasma–wall interaction, while the L-mode serves as a baseline with minimal tin radiation.

As mentioned above, the H-mode discharge exhibits transient ELM activity, which periodically increases particle and heat fluxes to the divertor targets and can enhance impurity sputtering and release from plasma-facing components. In ELMy H-mode plasmas, divertor conditions during ELM bursts can differ significantly from inter-ELM phases, with electron temperatures and heat fluxes increasing by more than an order of magnitude [14]. These transient events may therefore influence impurity sources and transport in the edge plasma. In particular, the presence of sputtered tin from the CPS could in principle affect tungsten erosion through cross-sputtering processes, since tin ions impacting tungsten surfaces may contribute to enhanced tungsten sputtering at other divertor locations. The modeling presented in this work does not attempt to resolve the fast time scale of individual ELM crashes or the detailed spatial redistribution of impurity sources during these events. Instead, the simulations interpret experimentally measured plasma profiles and radiation signals averaged over many ELM cycles and should therefore be regarded as representative of an ELM-averaged plasma state. A quantitative assessment of transient ELM-driven sputtering and possible tin-induced enhancement of tungsten erosion would require dedicated edge impurity transport modeling coupled with detailed divertor spectroscopy, which is beyond the scope of the present work but represents an important topic for future studies.

A direct comparison of the engineering parameters is shown in Fig. 2. In L-mode, the limited heat load resulted in negligible tin sources, and only background tungsten radiation was detected. In contrast, H-mode discharges exhibited clear tin radiation signatures, with droplet ejection near the LTM [10]. Similar liquid metal behavior has been reported in other devices under deuterium or hydrogen exposure, though with different CPS configurations ([15–17]), and its underlying mechanisms remain under investigation. Recent studies [18] show all the criticalities around the observed phenomena. Devices such as FTU, however, did not report droplet release under EU-DEMO-relevant heat loads (18 MW/m^2) in an L-mode discharge [5], highlighting the importance of modeling transport consistently with the experimental context.

The approach used for the modeling of the above mentioned discharges, relied on the usage of the ASTRA and the Aurora codes to simulate the relevant physical processes. Specifically, ASTRA was employed to model the core plasma behavior, leveraging on its integrated modeling capabilities to include turbulent and neoclassical transport mechanisms of both main plasma particles and impurities. The physical model implemented in ASTRA was validated against the experimental measurements of the analyzed shots, in terms of electron density and temperature profiles, as well as core radiated power, ensuring an accurate representation of the plasma conditions. Aurora, on the other hand, was utilized on a second stage, exploiting its capabilities of computing the transport equation for each charge states of impurity. Unlike ASTRA, Aurora computes the full density distribution

	L-mode	H-mode
Parameter	**#41271**	**#41279**
P_{ECRH} [MW]	0.9	4.3
P_{NBI} [MW]	0.0	2.6
$\overline{n}_e$ $[10^{19}\ m^{-3}]$	1.5	4.
I_P $[MA]$	0.8	1.0

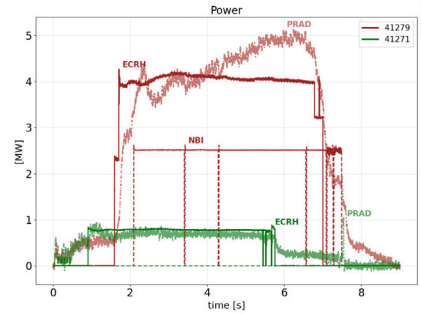

Fig. 2. Comparison of the engineering parameters of the two discharges is reported in the table. On the right-hand side, the plot shows the time evolution of the external heating power for the two discharges. The H-mode plasma is heated by both ECRH (solid) and NBI (dashed), whereas the L-mode discharge relies solely on ECRH. The corresponding total radiated power is also reported (dotted lines).

across all impurity charge states, rather than relying on the coronal equilibrium assumption. This distinction is particularly relevant for high-Z impurities such as tin or tungsten, whose radiation and transport properties depend sensitively on the detailed charge-state distribution. While the coronal approximation may provide a reasonable description in stationary core conditions, in edge regions – characterized by steep gradients – the coupled evolution of neighboring charge states can influence the impurity density profile and associated radiative losses. By resolving the full charge-state distribution, Aurora provides a more accurate description of impurity behavior and the associated radiated power, enabling also the possibility to validate the experimental results from the spectroscopy. Finally, a comparison between the impurity density profiles and radiated power obtained from both codes was performed, highlighting the strengths and limitations of each approach.

Based on these observations, the integrated impurity transport modeling was carried out for the H-mode case to identify the dominant transport mechanisms and verify whether impurity accumulation remains within acceptable operational limits. For the L-mode discharge, direct ion temperature measurements were unavailable; a reasonable profile was assumed to allow a self-consistent simulation focusing on tungsten, the only impurity experimentally detected. Additionally, a predictive cross-check was conducted by applying the same tin source derived from the H-mode case to the L-mode plasma configuration to assess whether a comparable impurity source could be tolerated in a lower confinement regime.

3.1. ASTRA and Aurora simulation setup

The ASTRA code [7,8] solves the 1.5D transport equation for electron and ion temperatures T_e, T_i, electron density n_e, and the poloidal flux Ψ, while updating the equilibrium configuration (2D), solving the Grad-Shafranov equation at each interaction through the SPIDER [19] magnetic equilibrium code called within ASTRA.

The quasi-neutrality condition is implemented to account for the presence of impurities in the evolution of the main plasma density and the neutral density is computed by considering ionization and recombination phenomena through an internal ASTRA subroutine (NEUT). In this framework, the impurity density distribution is computed assuming coronal equilibrium and the effective charge, Z_{eff}, is evaluated at each iteration updating the density of impurity and main ions.

The power balance considers all contributions from the main plasma and external sources, including radiated power from impurities and the main plasma (Bremsstrahlung and synchrotron radiation), Ohmic heating, collisional heat exchange, Neutral Beam Injection (NBI) (only for the H-mode case) and Electron Cyclotron Resonance Heating (ECRH).

Neoclassical and turbulent fluxes are computed respectively by FACIT [20,21] for the impurity and TGLF-SAT2 [22] for both the impurity and the main plasma. FACIT was employed to allow a more accurate description of the neoclassical transport of heavy impurity (Sn and W), explicitly accounting for poloidal asymmetries caused by strong toroidal rotation of the plasma.

In the ASTRA model, the impurity density and main plasma profiles evolve self-consistently in the computational domain from $\rho_{tor} = 0$ to $\rho_{tor} = 0.85$, where ρ_{tor} is the normalized plasma radius coordinate. This limit is mainly given by the difficulty of applying the TGLF-SAT2 transport model in the H-mode pedestal, therefore both plasmas have been treated in the same way with boundary condition at $\rho_{tor} = 0.85$. The domain used for the impurity density profile is extended to $\rho_{tor} = 1$, in order to capture the impurity behavior in the pedestal region, mainly for the neoclassical effects, acknowledging the limitations arising from the lack of a proper model for the turbulent transport within the pedestal. For the main plasma profiles, the quantities in the pedestal region are fixed to the experimental values.

Once the main characteristics of transport are analyzed by ASTRA, the Aurora code is used, to study the distribution of the different charge states of the impurity, overcoming the limitations given by the usage of an average value for the impurity charge assumed in the ASTRA modeling. In particular, Aurora solves the 1.5D impurity transport equation for each charge state of impurity, including ionization, recombination, and transport processes. The code makes use of a super-staging approach, grouping several charge states into a single stage to reduce computational complexity while maintaining accuracy: this is particularly useful for heavy impurities like tin. At the same time it allows us to compute the corresponding radiated power emitted by the different charge states and to also discriminate from the types of radiation. One drawback of the Aurora code is that it does not update the main plasma profiles self-consistently, as ASTRA does. Hence, the main plasma profiles are imposed as input to the code, and they remain fixed during the simulation.

An iterative loop has been implemented in order to match the experimental value of the total power radiated from the impurity, and the correspondent impurity source term has been updated, to finally compute the distribution of the various charge states as well as the total profile of the impurity density.

To this end, Aurora requires both the kinetic profiles and the transport coefficients to solve the impurity transport equations. The former are provided by the final simulated outputs from ASTRA, the latter are derived from the total neoclassical and turbulent fluxes computed, respectively, by FACIT and TGLF-SAT2 within ASTRA. This approach ensures a consistent treatment of transport and allows Aurora to fully exploit its capabilities in accurately computing the radiation and spatial distribution of impurities for each individual charge state.

A critical aspect in transitioning from the ASTRA impurity analysis to the Aurora framework is the treatment of the turbulent transport coefficients. In ASTRA, the turbulent flux is computed by the TGLF-SAT2 model, which outputs a flux density of the form:

$$\frac{\Gamma_{turb}}{n} = -D_{turb}\frac{\nabla n}{n} + V_{turb} \tag{1}$$

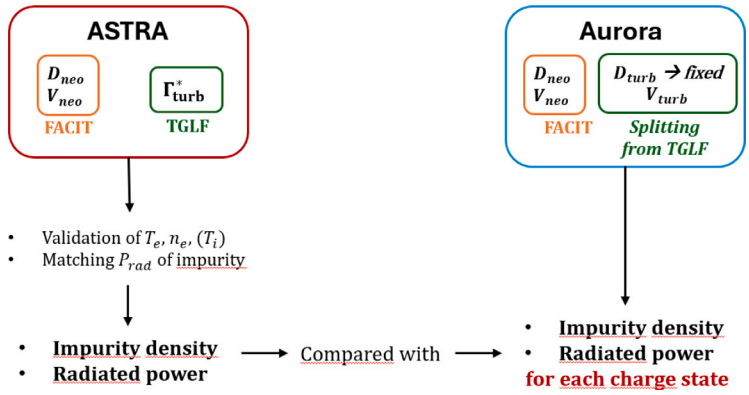

Fig. 3. Schematic representation of the workflow implemented.

where the quantity has the units of a convection velocity [m/s] but actually contains both diffusive and convective contributions. When an average impurity charge state is used, as in ASTRA, this approximation is generally sufficient because the transport of the bulk impurity density depends only on the total flux, and the internal redistribution among charge states is not resolved.

However, when solving for each charge state separately, as done in Aurora, it becomes important to explicitly separate the diffusive and convective components. This is because each charge state can experience different relative effects from diffusion and convection: higher charge states are more sensitive to convective transport, while lower charge states may be dominated by diffusion. Without this separation, the calculated spatial profiles of individual charge states could be inaccurate, which would propagate to errors in the predicted radiation and impurity distribution. Explicitly splitting diffusion and convection ensures that Aurora can properly account for the charge-state-dependent transport dynamics and provide a more accurate description of impurity behavior.

The separation of the diffusive and convective components is performed by deriving the turbulent convective velocity V_{turb} from Eq. (1), while assuming a constant turbulent diffusion coefficient $D_{turb} = 2\ \mathrm{m}^2/\mathrm{s}$. The turbulent particle flux density Γ_{turb}/n is taken directly from the TGLF-SAT2 output provided by ASTRA. Fixing D_{turb} allows V_{turb} to be determined consistently from the total turbulent particle flux predicted by TGLF, thereby preserving the overall transport balance obtained in the self-consistent ASTRA/TGLF modeling. Since the relative contribution of diffusive and convective transport influences the resulting impurity profile, a scan over D_{turb} values in the range $0.1 - - 5\ \mathrm{m}^2/\mathrm{s}$ was performed. The selected value of $2\ \mathrm{m}^2/\mathrm{s}$ provides the best agreement with the impurity density profiles obtained in ASTRA, while remaining within a physically reasonable range and consistent with the transport mechanisms identified in the self-consistent modeling.

In the following scheme (Fig. 3), a summary of the modeling strategy is reported.

The primary outcome of this modeling strategy includes the identification of the main transport mechanisms thanks to the ASTRA analysis and its validation against experimental profiles, as well as a prediction of impurity distribution in a self-consistent manner. Moreover, a more accurate estimate of the impurity radiated power and density distribution for the different charge states has been obtained leveraging on Aurora capabilities. The results of the impurity distribution and radiated power from the two codes can finally be compared to show the strengths and limiting factors of the modeling.

4. Results and discussion

This section presents the main results of the impurity transport model validation against experimental data. The validation approach, applied to both discharges investigated (#41279 H-mode and #41271 L-mode), is based on reproducing the impurity bolometric radiated power as well as the experimental electron density, electron temperature, and (for the H-mode case) ion temperature profiles. Additionally, the impurity density profile and the corresponding transport mechanisms have been evaluated from the simulation results, as no direct experimental measurements are available for comparison.

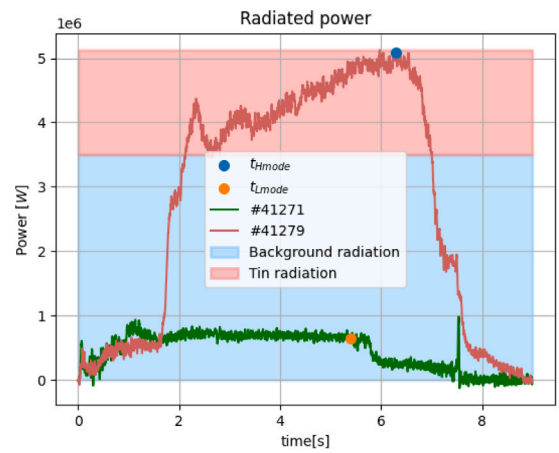

Fig. 4. Time evolution of the radiated power for both the shots (#41279 in red and #41271 in green). The blue and orange dots show the instant at which experimental values were extracted, representing the highest radiated powers reached during the discharges. The red area represents the fraction of power associated to tin radiation for the H-mode discharge, while the blue area is the "background radiation".

To quantify the amount of radiation attributable to impurities, data from the bolometers [12] were used to determine the total radiated power originating from different plasma regions. Fig. 4 shows the time evolution of this signal.

In the H-mode discharge (red line), the outer strike point (OSP) reaches the LTM shortly before 2 s. At this moment, a sudden rise in radiated power is observed, caused by the emission of impurities, mainly W, released from the module. At approximately 2.4 s, the OSP starts to be located directly on the probe, and the corresponding radiation level is interpreted as background radiation (main plasma + W + light impurities). Any additional radiation from this moment on is therefore attributed solely to tin. The model validation is carried out at the time of maximum radiation: around 6.3 s for the H-mode (blue dot in Fig. 4) and 5.6 s for the L-mode (yellow dot). For the H-mode discharge, subtracting the background radiation (3.5 MW) from the total radiation at 6.3 s (5 MW) gives 1.5 MW of Sn radiation. In contrast, for the L-mode case, no Sn radiation is detected: the injected power was insufficient to sputter Sn from the probe. The observed radiation (0.63 MW) is therefore attributed solely to W contamination.

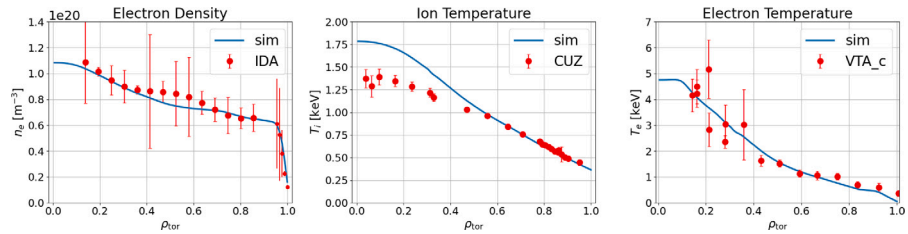

Fig. 5. Experimental (red) and simulated (blue) profiles for discharge #41279 (H-mode). Electron density and temperature profiles are compared to Thomson scattering signals. For the former the signal is fitted with the IDA algorithm [23], for the latter, signal directly from the diagnostic (VTA in AUG [24]) is used. Ion temperature is compared with the charge exchange recombination spectroscopy (CUZ in AUG).

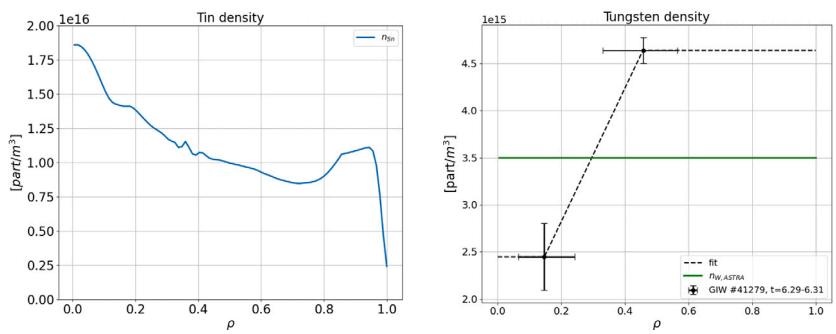

(a) (b)

Fig. 6. Tin density (a) as computed by ASTRA, and tungsten density (b) as experimentally detected (black dashed line) and as set in ASTRA (green).

With these radiated power targets, the ASTRA simulations were initialized as described in Chapter 3, using the experimental main plasma profiles as initial conditions and an initial guess for the impurity density proportional to the electron density. Only Sn was simulated for the H-mode, and W is added with a constant concentration in order to reach the experimental background radiation (3.5 MW) together with the Bremmstrhalung component, whereas only W is modeled for the L-mode. The impurity concentration (of Sn for H-mode and W for the L-mode) was then iteratively adjusted to match the experimentally inferred radiated power.

The next sections analyze the results for the H-mode and L-mode scenarios, followed by a prediction of a L-mode case with a Sn concentration comparable to that of the H-mode discharge.

4.1. H-mode scenario (#41279)

Fig. 5 compares the ASTRA steady-state profiles to the experimental measurements. As detailed in Section 3.1, TGLF-SAT2 is applied in the region $\rho \leq 0.85$, which defines the outer boundary of the self-consistent transport calculation. For $\rho > 0.85$, the kinetic profiles are prescribed to match the experimental pedestal measurements.

The validation shows a good agreement between simulated electron temperature and density profiles against core Thomson scattering signals. Ion temperature, on the other hand, exhibits a higher discrepancy in the core. One of the reasons can be found in the limitations of TGLF-SAT2's ion flux predictions in this very central region. Moreover, in this ASTRA simulations, the modeling of sawteeth is neglected, and this phenomenon can lead to the flattening of the temperatures.

Tin radiation has been matched, setting a value of $n_{Sn} = 1.4 \cdot 10^{-4} \cdot n_e$ as boundary condition for the impurity density equation at $\rho = 1.0$. The correspondent impurity profile modeled by ASTRA is reported in Fig. 6(a). The tungsten profile used in the ASTRA simulation is also shown in Fig. 6(b) for completeness. The black dashed line represents the fit through the two points where the spectrometer (GIW - Grazing Incidence Spectrometer in AUG [13]) inferred the W concentration. In ASTRA, an average value between these two points was therefore adopted, resulting in a corresponding radiation level of approximately 1 MW. The remaining background radiation (2.5 MW) is mainly attributed to light impurities and Bremsstrahlung radiation.

The profile shows a clear core peaking driven by the neoclassical pinch, in line with theoretical expectations for high-Z impurities [25–27].

The effective charge profile obtained from ASTRA yields a central value of $Z_{eff} \approx 1.3$. The dominant contribution arises from tin impurities. For an average concentration c_{Sn} $(= n_{Sn}/n_e) \approx 1.45 \cdot 10^{-4}$ and a charge value Z_{Sn} that goes from 40 in the core to 20 at the pedestal top, tin increases the effective charge by $\Delta Z_{eff} \approx 0.21 - 0.27$ in the plasma core, decreasing towards ≈ 0.05 near the pedestal top due to the lower local electron temperature. The corresponding radial profile of Z_{eff} therefore peaks in the plasma center and approaches values close to unity towards the edge. Tungsten is present at a lower concentration, $c_W \approx 4 \cdot 10^{-5}$, with a slightly higher charge value of $Z_W \approx 47$ in the core. As a result, tungsten provides a smaller yet non-negligible contribution to the total effective charge. Despite the high charge states of both heavy impurities, their relatively low concentrations ensure that the overall Z_{eff} remains moderate across the plasma radius.

Toroidal rotation produced by co-current NBI injection is also included in the simulations. The measured rotation profile is centrally hollow, due to the combination of limited beam central penetration at high density and strong central ECRH [28]. The measured rotation profile has been prescribed in the simulations and the corresponding profile is shown in Fig. 7(a), together with the main ion Mach number 7(b) and the impurity effective Mach number $M_z^* = \left(\left(\frac{A}{A_i} - \frac{Z}{Z_i}\frac{Z_{eff}}{Z_{eff}+T_i/T_e}\right) M_i\right)^{1/2}$ 7(c), as defined in [20]. Its central value around 0.15 is low enough to not have any practical impact on the neoclassical transport of tin, whereas the peripheral value reaching 0.6 has a non-negligible impact.

Therefore the central impurity peaking which results from the simulation and which is shown in Fig. 6(a) is mainly produced by the peaked main ion density profile, partly reinforced by the increased level of neoclassical transport and the reduced temperature screening around

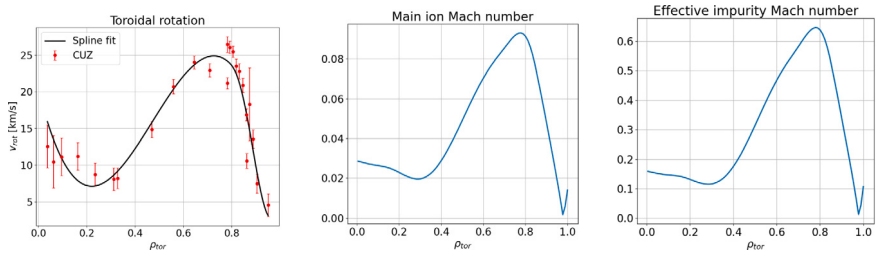

(a) (b) (c)

Fig. 7. Toroidal rotation velocity (a), main ion Mach number (b), and effective impurity Mach number (c) profiles.

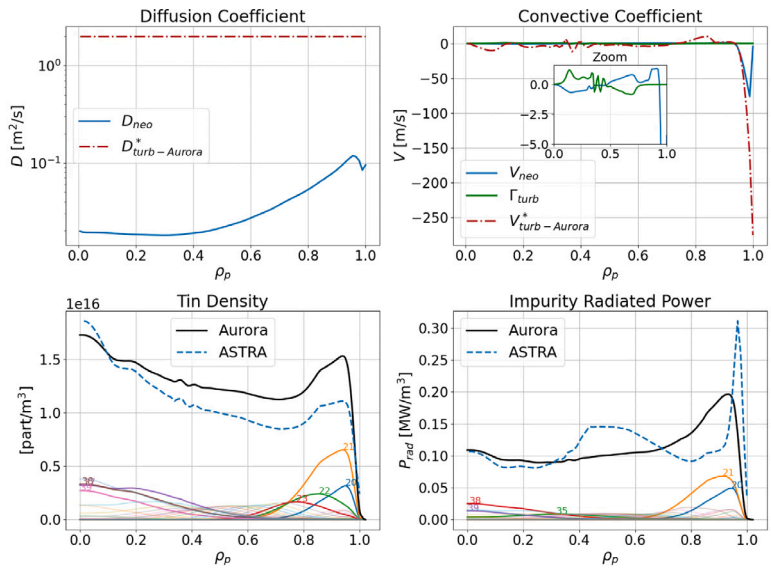

Fig. 8. From left to right, top: diffusion coefficients, convection coefficients. Bottom: tin density profile and power density profiles of ASTRA and Aurora.

mid-radius. The local hollow profile at around $\rho = 0.8$, in contrast, is produced by the flatter density profile in this region, where temperature screening can still prevail.

A well-defined pedestal forms at the edge due to the strong neoclassical inward convection there. In this region ($\rho > 0.85$), only neoclassical transport is computed, while turbulence is neglected, due to the limitation of the TGLF-SAT2 code previously mentioned. Transport mechanisms of the impurities in the pedestal region are still unknown, a potentially beneficial outward turbulent flux could be present or not. A hollow region appears around $\rho \approx 0.7$, caused by a local reversal of the total convective velocity. In this radial location, it is possible to notice a flatter electron density profile, compared to the ion temperature, and this could lead to a locally hollow impurity profile.

After obtaining an initial estimate of the impurity profile with ASTRA, a more detailed analysis was performed with Aurora. ASTRA profiles for the kinetic parameters were used as inputs for Aurora, while transport coefficients were set as described in Section 3. Aurora then calculates the full impurity profiles, including both density and radiated power. A summary of the results is shown in Fig. 8.

The top row of Fig. 8 shows the transport coefficients. Neoclassical coefficients (blue lines), computed with FACIT, are the same in both ASTRA and Aurora. Turbulent coefficients differ between the two codes, as explained in Section 3: in ASTRA, the turbulent flux is entirely treated as a convective flux (green line), whereas in Aurora, a diffusive component is imposed (red dashed line, top right), and the convective component is computed accordingly (red dashed line, top left).

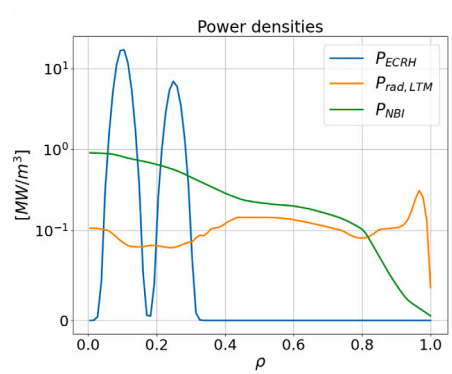

Fig. 9. Comparison of injected power from both NBI and ECRH system, and radiated power emitted from Sn by the LTM.

The impurity density profile (bottom left) from Aurora closely resembles the ASTRA profile, consistent with the use of the same transport. Small differences can be understood by examining the radiated power profiles (bottom right). Both codes predict a total Sn radiated power of ≈ 1.5 MW, in agreement with experiment. However, Aurora predicts a less pronounced peak in the edge region. This difference arises because ASTRA assumes coronal equilibrium with an average charge state, while Aurora accounts for atomic processes for each charge state, which are more important at the edge. Consequently, slightly different particle concentrations are required to achieve the

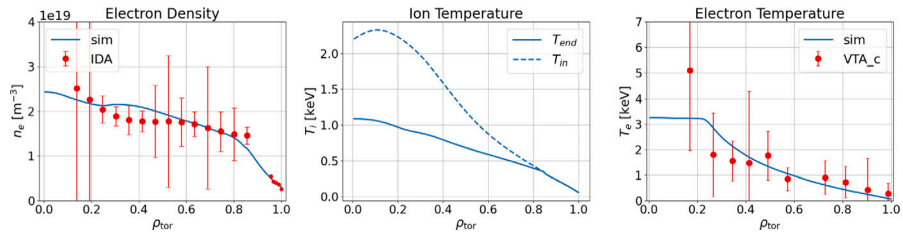

Fig. 10. Computed vs. measured profiles for shot #41271, L-mode. The green dashed line one the right plot, represents the assumed ion temperature profile.

same radiated power, explaining the minor differences in the impurity profiles. To be noted is how the radiated power density peaks in the edge region, where it is less dangerous in terms of core plasma performance degradation. Nevertheless, the total radiated power remains significant due to the high impurity concentration.

With the Aurora modeling, it is also possible to verify the experimental observation of [10], showing that the most abundant species are Sn^{20+} to Sn^{21+} cumulating in the edge region, while higher charge states (Sn^{35+}, Sn^{38+}, Sn^{39+}) peak in the core.

Once the impurity distribution is determined, the radiated power can be compared with the injected heating power to evaluate the risk of radiative collapse (Fig. 9). During the experimental campaign, only a small test-box was installed in the divertor. This box corresponds to approximately 4% of the surface area of a single divertor tile. While ASDEX Upgrade features 128 divertor tiles in total, the plasma interacts only with a narrow footprint on each tile. Extrapolating the measured Sn radiated power from the test module to this footprint across all tiles results in radiated power values that already exceed the total heating power of the discharge. Even when considering that the interaction occurs only within the plasma footprint, such a linear scaling is clearly unphysical. This simple extrapolation should therefore be interpreted as a conservative upper bound. In reality, a large Sn source would strongly cool the plasma and modify the divertor conditions, leading to a reduction of the impurity release and a self-limiting behavior of the radiation. Furthermore, as discussed in [10], the large Sn source observed in the present experiment is associated with the unintended emission of liquid-metal droplets from the test module. Whether a liquid-Sn divertor can operate without such droplet formation remains an open question, and mitigation strategies may be required to prevent excessive impurity release.

4.2. L-mode scenario (#41271)

The analysis for the L-mode discharge follows a similar approach, starting with the validation of the model with ASTRA and then performing a more detailed impurity transport analysis with Aurora. Since no NBI heating was applied in this case, no charge exchange recombination spectroscopy measurements and therefore no ion temperature and toroidal rotation profiles are available. Therefore, a plausible ion temperature profile was assumed for the initial condition on the ASTRA modeling, based on a typical ratio with the electron temperature, as follows: $T_i(\rho, t = 0) = T_e(\rho, t = 0) \cdot (0.5 + 0.5 \cdot \rho)$. Then all the profiles have been evolved along the simulation. Given the already very low rotation of the H-mode case with an applied NBI torque, for this L-mode case, in which no NBI is applied and no rotation profile measurement is available, a profile of zero toroidal rotation has been assumed. Intrinsic rotation is observed in ASDEX Upgrade in the conditions of this L-mode plasma with ECRH only [29], but regularly with very low levels of Mach numbers for which no significant impact on the tungsten neoclassical transport can be expected. In any case, the assumption of zero toroidal rotation could lead to a small underestimation of the neoclassical transport contribution.

Final and experimental profiles are shown in Fig. 10 for electron density and temperature, for the ion temperature, the initial and final profiles are reported.

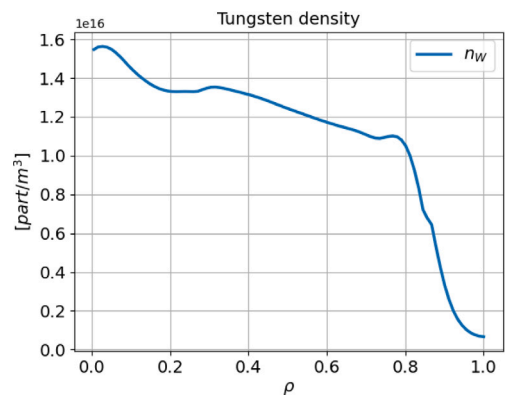

Fig. 11. Tungsten density profile as computed by ASTRA with the coronal equilibrium assumption.

ASTRA simulations shows a rather flat electron density profile 10 (left), reflecting the expected turbulence-dominated transport in L-mode, with central electron heating at low density [30]. Notably, the electron density is nearly an order of magnitude lower than in the H-mode case, leading to very low collisionality and a decoupling of ion and electron temperatures. Overall, the agreement between simulated and experimental profiles is satisfactory, assessing the pretty high uncertainties in particular of the Thomson scattering measurements (via VTA [24]) in the core region.

For the impurity transport analysis, only tungsten was considered, as no tin radiation was detected experimentally. The tungsten density profile computed by ASTRA is shown in Fig. 11.

The profile displays an almost flat shape in the central region, a signature of transport dominated by turbulence. In this scenario, the typical turbulent outward flux counteracts the neoclassical inward pinch, yielding a nearly uniform tungsten distribution. On the other hand, the accumulation of W at the edge is driven by the neoclassical inward convection, since no turbulent transport is considered in this region (TGLF-SAT2 is only applied up to $\rho = 0.85$).

This profile matched the 0.63 MW of W radiation detected by theBPT diagnostic with a value of $n_W = 2 \cdot 10^{-4} \cdot n_e$ set at the boundary ($\rho = 1.0$).

Similarly to the H-mode case, in Fig. 12, coefficients and tungsten density and radiation profiles computed by Aurora are compared with the ASTRA result.

Once the analysis on the impurity transport is completed, the radiated power from tungsten can be compared with the injected heating power to evaluate the impact on plasma performance. The resulting power density profiles (Fig. 13) show that tungsten radiation remains low, consistent with the low central density in L-mode which limits the core radiation. No extrapolation to a full CPS-like divertor has been performed in this case, as the resulting tungsten radiation is already the total detected during the discharge.

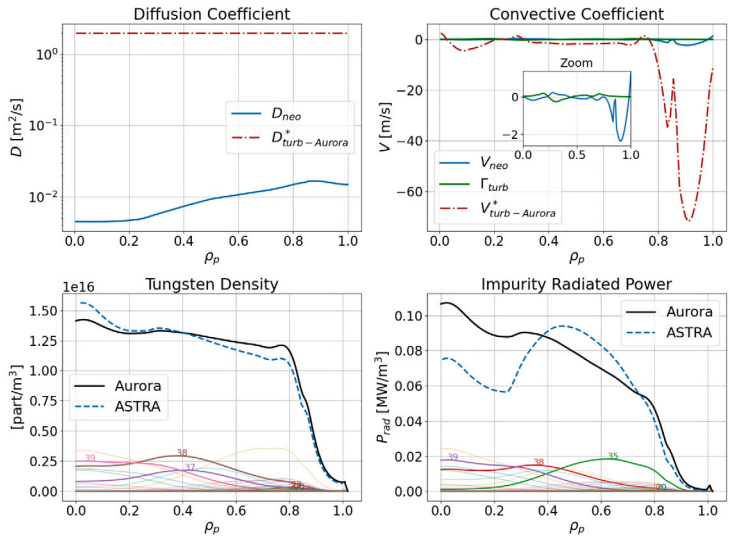

Fig. 12. From left to right, top: diffusion coefficients, convection coefficients. Bottom: tin density profile and power density profiles of ASTRA and Aurora.

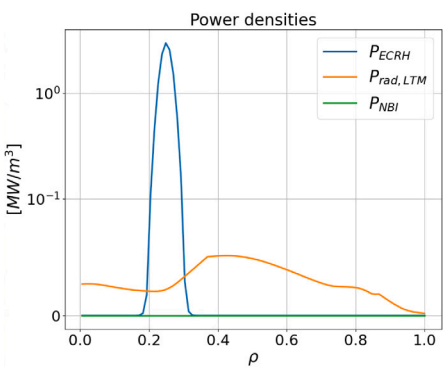

Fig. 13. Power densities profiles of ECRH and radiated power from Tungsten.

4.3. Prediction of an L-mode scenario with high Sn radiation

It was considered informative to also investigate the impact of tin injection in an L-mode scenario. A simulation was performed using the same tin source adopted in the H-mode case ($n_W = 1.4 \cdot 10^{-4} \cdot n_e$), applied here as a boundary condition while using the L-mode main plasma profiles (n_e, T_e, and T_i).

In Fig. 14, a comparison of the profiles considered interesting for the analysis is shown. The tin density profiles (first plot) resembles the electron ones (second plot), both in terms of magnitude and peaking. Being the electron density significantly lower in L-mode, the resulting tin concentration (third plot) at the end of the simulation is instead almost four times higher than in the H-mode case. However, the radiated power (fourth plot) remains considerably lower, mainly due to the strong dependence on the electron density. This outcome highlights the crucial role of background plasma conditions in determining impurity accumulation and radiation levels.

The comparison between the radiated power from the impurity and the injected heating power (Fig. 15) shows that the former remains significantly lower than in H-mode, even when assuming a "full CPS-like divertor" configuration. This directly results from the strong dependence of P_{rad} on both impurity and electron densities which are substantially lower in L-mode. Nevertheless, even in this scenario, extrapolating to a full CPS-like divertor yields a radiated power that would exceed the heating capabilities of ASDEX Upgrade. This represents a conservative upper bound, as plasma cooling and changes in divertor conditions would limit the impurity source and prevent such physically unrealistic values from being reached.

5. Conclusions

This work presented a modeling interpretation of the experiment exposing a Liquid Tin Module (LTM) to a diverted plasma in the ASDEX Upgrade tokamak. The study focused on understanding the transport of tin impurities in the core, estimating the resulting contamination levels. Two discharges were analyzed: an L-mode and an H-mode, with the latter exhibiting significant tin radiation signatures. The modeling strategy employed two different codes, ASTRA and *Aurora*: the former was employed to interpret and reconstruct the plasma and impurity transport mechanisms, the latter to precisely reconstruct the radiation and impurity density distributions for each charge states.

The H-mode discharge showed clear tin radiation signatures, with droplet ejection near the LTM, while the L-mode discharge exhibited negligible tin sources. The modeling results indicated that in the H-mode scenario, the tin concentration in the core plasma reached levels of approximately $1 \cdot 10^{-4}$, leading to a substantial (and unbearable) radiated power fraction. In the L-mode scenario, modeling predicts a lower core accumulation, mainly due to the flatter electron density profile, in combination with the lower rotation, in the absence of NBI. Although the tin concentration remains relatively high, the resulting radiation is partially mitigated by the reduced electron density. Nevertheless, the radiated power remains significant and still above acceptable limits. In both regimes, droplet ejection is the dominant concern: large bursts of tin can trigger excessive radiation levels regardless of confinement mode.

From a divertor design perspective, extrapolating the measured tin source to a full CPS-like divertor configuration suggests that radiated power could exceed acceptable thresholds unless droplet ejection is effectively controlled. These findings indicate that liquid-tin divertors could remain compatible with acceptable core plasma performance, provided that turbulent transport can counteract neoclassical inward convection and – most critically – that impurity bursts driven by droplet ejection are suppressed. To confirm the viability of such systems under reactor-relevant conditions, dedicated experimental campaigns with CPS-based tin divertor modules are required, with particular emphasis on developing and validating robust mitigation strategies for droplet ejection.

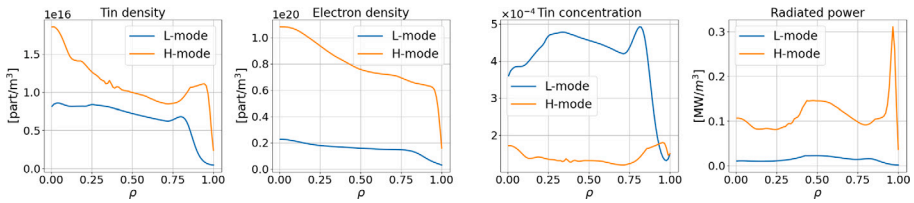

Fig. 14. From left to right: tin density profile, electron density profile, tin concentration, and radiated power density. In orange the H-mode, in blue the L-mode.

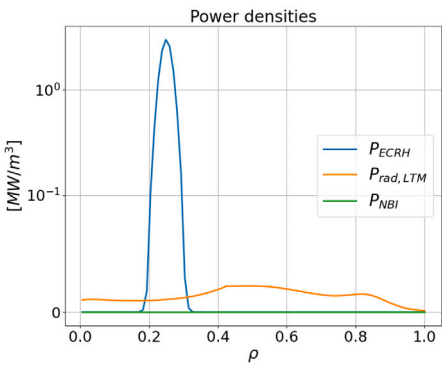

Fig. 15. Comparison of auxiliary power and radiated power from tin for the L-mode scenario with tin.

CRediT authorship contribution statement

Elisabetta Bray: Writing – original draft, Methodology, Conceptualization. **Daniel Fajardo:** Methodology, Conceptualization. **Clemente Angioni:** Writing – original draft, Supervision, Conceptualization. **Oleg Samoylov:** Data curation, Conceptualization. **Ralph Dux:** Supervision, Conceptualization. **Giuseppe F. Nallo:** Supervision, Conceptualization. **Chiara Marchetto:** Supervision. **Fabio Subba:** Supervision.

Declaration of competing interest

The authors declare that they have no known competing financial interests or personal relationships that could have appeared to influence the work reported in this paper.

Acknowledgments

This publication is part of the project PNRR-NGEU which has received funding from the MUR-DM 118/2023

Data availability

Data will be made available on request.

References

[1] R.E. Nygren, F.L. Tabarés, Liquid surfaces for fusion plasma facing components—A critical review. part I: Physics and PSI, Nucl. Mater. Energy 9 (2016) 6–21, http://dx.doi.org/10.1016/j.nme.2016.08.008, URL https://www.sciencedirect.com/science/article/pii/S2352179115301307.

[2] T.W. Morgan, P. Rindt, G.G. van Eden, V. Kvon, M.A. Jaworksi, N.J.L. Cardozo, Liquid metals as a divertor plasma-facing material explored using the Pilot-PSI and Magnum-PSI linear devices, Plasma Phys. Control. Fusion 60 (1) (2017) 014025, http://dx.doi.org/10.1088/1361-6587/aa86cd, Publisher: IOP Publishing.

[3] P. Rindt, J.L. van den Eijnden, T.W. Morgan, N.J. Lopes Cardozo, Conceptual design of a liquid-metal divertor for the European DEMO, Fusion Eng. Des. 173 (2021) 112812, http://dx.doi.org/10.1016/j.fusengdes.2021.112812, URL https://www.sciencedirect.com/science/article/pii/S0920379621005883.

[4] S. Roccella, G. Dose, R. de Luca, M. Iafrati, A. Mancini, G. Mazzitelli, CPS based liquid metal divertor target for EU-DEMO, J. Fusion Energy 39 (6) (2020) 462–468, http://dx.doi.org/10.1007/s10894-020-00263-4.

[5] G. Mazzitelli, M. Apicella, M. Iafrati, G. Apruzzese, F. Bombarda, F. Crescenzi, L. Gabellieri, A. Mancini, M. Marinucci, A. Romano, t.F. Team, Experiments on the frascati tokamak upgrade with a liquid tin limiter, Nucl. Fusion 59 (9) (2019) 096004, http://dx.doi.org/10.1088/1741-4326/ab1d70, Publisher: IOP Publishing.

[6] M. Jaworski, T. Abrams, J. Allain, M. Bell, R. Bell, A. Diallo, T. Gray, S. Gerhardt, R. Kaita, H. Kugel, B. LeBlanc, R. Maingi, A. McLean, J. Menard, R. Nygren, M. Ono, M. Podesta, A. Roquemore, S. Sabbagh, F. Scotti, C. Skinner, V. Soukhanovskii, D. Stotler, t.N. Team, Liquid lithium divertor characteristics and plasma–material interactions in NSTX high-performance plasmas, Nucl. Fusion 53 (8) (2013) 083032, http://dx.doi.org/10.1088/0029-5515/53/8/083032, Publisher: IOP Publishing and International Atomic Energy Agency.

[7] E. Fable, C. Angioni, F.J. Casson, D. Told, A.A. Ivanov, F. Jenko, R.M. McDermott, S.Y. Medvedev, G.V. Pereverzev, F. Ryter, W. Treutterer, E. Viezzer, t.A.U. Team, Novel free-boundary equilibrium and transport solver with theory-based models and its validation against ASDEX upgrade current ramp scenarios, Plasma Phys. Control. Fusion 55 (12) (2013) 124028, http://dx.doi.org/10.1088/0741-3335/55/12/124028, Publisher: IOP Publishing.

[8] G.V. Pereverzev, P.N. Yushmanov, ASTRA Automated System for TRansport Analysis.

[9] F. Sciortino, T. Odstrčil, A. Cavallaro, S.P. Smith, O. Meneghini, R. Reksoatmodjo, O. Linder, J.D. Lore, N.T. Howard, E.S. Marmar, S. Mordijck, Modeling of particle transport, neutrals and radiation in magnetically-confined plasmas with Aurora, Plasma Phys. Control. Fusion 63 (11) (2021) 112001, http://dx.doi.org/10.1088/1361-6587/ac2890, Publisher: IOP Publishing.

[10] J. Scholte, M. Balden, D. Brida, J. Cecrdle, R. Dux, S. Elgeti, M. Faitsch, A. Herrmann, J. Horacek, K. Hunger, K. Krieger, A. Manhard, P. De Marné, V. Rohde, T. Morgan, Performance of a liquid Sn divertor target during ASDEX upgrade L-mode and H-mode operation, Nucl. Mater. Energy 37 (2023) 101522, http://dx.doi.org/10.1016/j.nme.2023.101522, URL https://linkinghub.elsevier.com/retrieve/pii/S2352179123001618.

[11] J.G.A. Scholte, M. Iafrati, S.S.H. Lam, B. Tyburska-Pueschel, M. Riepen, F. Brochard, M.M.P. Vissers, T.W. Morgan, Reducing tin droplet ejection from capillary porous structures under hydrogen plasma exposure in Magnum-PSI, Nucl. Mater. Energy 34 (2023) 101315, http://dx.doi.org/10.1016/j.nme.2022.101315, URL https://www.sciencedirect.com/science/article/pii/S235217912200196X.

[12] P. David, M. Bernert, T. Pütterich, C. Fuchs, S. Glöggler, T. Eich, t.A.U. Team, Optimization of the computation of total and local radiated power at ASDEX Upgrade, Nucl. Fusion 61 (6) (2021) 066025, http://dx.doi.org/10.1088/1741-4326/abf2e1, Publisher: IOP Publishing.

[13] R.J. Fonck, A.T. Ramsey, R.V. Yelle, Multichannel grazing-incidence spectrometer for plasma impurity diagnosis: SPRED, Appl. Opt. 21 (12) (1982) 2115–2123, http://dx.doi.org/10.1364/AO.21.002115.

[14] J. Cecrdle, J.G.A. Scholte, J. Horacek, T.W. Morgan, K. Krieger, H. Greuner, B. Böswirth, A. Manhard, D. Tskhakaya, M. Faitsch, Predictive and interpretative modelling of ASDEX-upgrade liquid metal divertor experiment, Fusion Eng. Des. 194 (2023) 113886, http://dx.doi.org/10.1016/j.fusengdes.2023.113886, URL https://www.sciencedirect.com/science/article/pii/S0920379623004684.

[15] W. Ou, F. Brochard, T. Morgan, Bubble formation in liquid Sn under different plasma loading conditions leading to droplet ejection, Nucl. Fusion 61 (6) (2021) 066030, http://dx.doi.org/10.1088/1741-4326/abf9e0, Publisher: IOP Publishing.

[16] A. Manhard, T. Schwarz-Selinger, M. Balden, T. Dürbeck, H. Maier, R. Neu, Deuterium retention in solid and liquid tin after low-temperature plasma exposure, Nucl. Fusion 60 (10) (2020) 106007, http://dx.doi.org/10.1088/1741-4326/aba801, Publisher: IOP Publishing.

[17] A. Manhard, Stabilization of liquid tin surfaces under d plasma irradiation by a capillary porous system, Nucl. Mater. Energy 40 (2024) 101696, http://dx.doi.org/10.1016/j.nme.2024.101696, URL https://www.sciencedirect.com/science/article/pii/S2352179124001194.

[18] J.G.A. Scholte, R.S. Al, D. Horsely, M. Iafrati, A. Manhard, E. Martelli, M. Morbey, S. Roccella, J.W.M. Vernimmen, T.W. Morgan, Liquid metal droplet ejection through bubble formation under hydrogen plasma and radical exposure, J. Fusion Energy 44 (1) (2025) 22, http://dx.doi.org/10.1007/s10894-025-00492-5.

[19] SPIDER code - axisymmetric fixed boundary plasma equilibrium solver, URL https://www.keldysh.ru/papers/2006/prep07/prep2006_07.html.

[20] D. Fajardo, C. Angioni, F.J. Casson, A.R. Field, P. Maget, P. Manas, t.A.U. Team, J.E.T. Contributors, Analytical model for the combined effects of rotation and collisionality on neoclassical impurity transport, Plasma Phys. Control. Fusion 65 (3) (2023) 035021, http://dx.doi.org/10.1088/1361-6587/acb0fc, Publisher: IOP Publishing.

[21] D. Fajardo, C. Angioni, P. Maget, P. Manas, Analytical model for collisional impurity transport in tokamaks at arbitrary collisionality, Plasma Phys. Control. Fusion 64 (5) (2022) 055017, http://dx.doi.org/10.1088/1361-6587/ac5b4d, Publisher: IOP Publishing.

[22] G. Staebler, E.A. Belli, J. Candy, J. Kinsey, H. Dudding, B. Patel, Verification of a quasi-linear model for gyrokinetic turbulent transport, Nucl. Fusion 61 (11) (2021) 116007, http://dx.doi.org/10.1088/1741-4326/ac243a, Publisher: IOP Publishing.

[23] Z. Liu, Z. Luo, T. Wang, Y. Huang, Y. Wang, Q. Yu, W. Rui, Q. Yuan, B. Xiao, J. Li, Plasma profile tomography for EAST based on integrated data analysis, Plasma Phys. Control. Fusion 64 (9) (2022) 094001, http://dx.doi.org/10.1088/1361-6587/ac83a3, Publisher: IOP Publishing.

[24] R.C. Isler, An overview of charge-exchange spectroscopy as a plasma diagnostic, Plasma Phys. Control. Fusion 36 (2) (1994) 171, http://dx.doi.org/10.1088/0741-3335/36/2/001.

[25] C. Angioni, M. Sertoli, R. Bilato, V. Bobkov, A. Loarte, R. Ochoukov, T. Odstrcil, T. Pütterich, J. Stober, T.A.U. Team, A comparison of the impact of central ECRH and central ICRH on the tungsten behaviour in ASDEX Upgrade H-mode plasmas, Nucl. Fusion 57 (5) (2017) 056015, http://dx.doi.org/10.1088/1741-4326/aa6453, Publisher: IOP Publishing.

[26] C. Angioni, T. Gamot, G. Tardini, E. Fable, T. Luda, N. Bonanomi, C. Kiefer, G. Staebler, The Asdex Upgrade Team, The EUROfusion Mst1 Team, Confinement properties of L-mode plasmas in ASDEX upgrade and full-radius predictions of the TGLF transport model, Nucl. Fusion 62 (6) (2022) 066015, http://dx.doi.org/10.1088/1741-4326/ac592b, URL https://iopscience.iop.org/article/10.1088/1741-4326/ac592b, Publisher: IOP Publishing.

[27] F.J. Casson, C. Angioni, E.A. Belli, R. Bilato, P. Mantica, T. Odstrcil, T. Pütterich, M. Valisa, L. Garzotti, C. Giroud, J. Hobirk, C.F. Maggi, J. Mlynar, M.L. Reinke, J.E. Contributors, A.-U. Team, Theoretical description of heavy impurity transport and its application to the modelling of tungsten in JET and ASDEX upgrade, Plasma Phys. Control. Fusion 57 (1) (2014) 014031, http://dx.doi.org/10.1088/0741-3335/57/1/014031, Publisher: IOP Publishing.

[28] R.M. McDermott, C. Angioni, R. Dux, A. Gude, T. Pütterich, F. Ryter, G. Tardini, t.A.U. Team, Effect of electron cyclotron resonance heating (ECRH) on toroidal rotation in ASDEX Upgrade H-mode discharges, Plasma Phys. Control. Fusion 53 (3) (2011) 035007, http://dx.doi.org/10.1088/0741-3335/53/3/035007.

[29] C. Angioni, A.G. Peeters, G.V. Pereverzev, F. Ryter, G. Tardini, Density peaking, anomalous pinch, and collisionality in tokamak plasmas, Phys. Rev. Lett. 90 (20) (2003) 205003, http://dx.doi.org/10.1103/PhysRevLett.90.205003, URL https://link.aps.org/doi/10.1103/PhysRevLett.90.205003.

[30] C. Angioni, A.G. Peeters, X. Garbet, A. Manini, F. Ryter, A.U. Team, Density response to central electron heating: theoretical investigations and experimental observations in ASDEX Upgrade, Nucl. Fusion 44 (8) (2004) 827, http://dx.doi.org/10.1088/0029-5515/44/8/003.